Progress In Electromagnetics Research, Vol. 114, 89–111, 2011

CALIBRATION OF SPACEBORNE LINEARLY POLARIZED LOW FREQUENCY SAR USING POLARIMETRIC SELECTIVE RADAR CALIBRATORS

J. Chen

School of Electronics and Information Engineering
Beihang University, Beijing 100191, China

S. Quegan

School of Mathematics and Statistics
University of Sheffield, Sheffield S3 7RH, UK

X. J. Yin

School of Electronics and Information Engineering
Beihang University, Beijing 100191, China

Abstract—Spaceborne synthetic aperture radar (SAR) systems operating at lower frequencies, such as P-band, are significantly affected by Faraday rotation (FR) effects. This paper presents a novel algorithm for measuring system errors (channel imbalance and cross-talk) in the presence of Faraday rotation for spaceborne polarimetric SAR data. It uses four polarimetric selective calibrators (four polarimetric active radar calibrators [PARCs] or possibly two PARCs and two gridded trihedrals). Theoretical analysis and simulations demonstrate that the optimized calibration scheme puts tight constraints on the accuracy of the associated Faraday rotation if the cross-talk is to be accurately measured. There are also strong constraints on the allowable signal-to-noise ratio and average polarimetric noise associated with the calibration devices. The analysis suggests that, unless the calibration sites are at the magnetic equator, independent measurements of total electron content (TEC) from a direct ground-satellite line-of-sight dual-frequency system are also needed.

Received 18 January 2011, Accepted 16 February 2011, Scheduled 19 February 2011
Corresponding author: Jie Chen (chenjie@buaa.edu.cn).

1. INTRODUCTION

The European Space Agency (ESA) is currently conducting Phase-A studies for the BIOMASS mission, which will measure global forest biomass and contribute to better understanding of the global carbon cycle [1]. The mission is based on a P-band polarimetric SAR, and one requirement for its success is that the data should be calibrated in order to remove system effects, such as channel imbalance and cross-talk. Accurate calibration is one of the most important issues for a radar system [2–11]. For polarimetric systems, several successful calibration approaches are available based on the properties of distributed targets and calibration devices [7–11]. Though these methods were originally developed for airborne systems, they are also applicable to satellite systems, but encounter problems at long wavelengths because of complications arising from Faraday rotation (FR). This may not be a serious issue even for frequencies as low as L-band, such as the ALOS-PALSAR system [12–21], but at P-band it becomes a serious issue [22–26]. Fortunately, spaceborne SAR systems are much more stable than airborne systems, and scene-by-scene updates of the system errors are unlikely to be required [26]. Instead, it should be sufficient to measure the system errors (i.e., channel imbalance and cross-talks) at instrumented calibration sites, and then apply these estimated errors to multiple scenes.

However, the measurements from these sites will be corrupted by FR, and it is necessary to estimate FR as part of estimating the radar system errors, since these two sources of error interact. Freeman investigated the calibration of polarimetric SAR using active radar calibrators [7, 8], and there are several recent studies about the calibration of both FR and radar system errors for ALOS-PALSAR [13–20].

This paper proposes a novel algorithm for calibrating a polarimetric low-frequency spaceborne SAR using a set of polarimetric selective radar calibrators, which can all be active or a combination of active and passive. Throughout the paper we assume a radar system operating in the horizontal-vertical polarization reference frame, and introduce the corresponding system model in Section 2. Section 3 derives the full solution for estimating both FR and the radar system errors. The statistics of the estimation errors in these terms are investigated in Section 4, both without and with disturbances (polarimetric noise from the calibrators, system noise and ambiguities). The values of FR derived using the calibrators are found to be insufficiently accurate to provide accurate estimates of cross-talk, unless polarimetric noise is very small and the signal-to-noise ratio

(SNR) is vary high. Two approaches to circumventing this problem are discussed in Section 5, together with our summary and conclusions.

2. POLARMETRIC SYSTEM MODEL

2.1. Faraday Rotation

When a polarized electromagnetic wave traverses the ionosphere, its interaction with free electrons and the Earth's magnetic field leads to rotation of the polarization vector [12, 21]. This phenomenon is known as Faraday rotation. The one-way FR for a SAR signal can be approximated as [21],

$$\Omega = \frac{K}{f_0^2} \cdot \left[B \cos\psi \cdot \sec\theta\right]_{400} \cdot \mathrm{TEC} \tag{1}$$

where Ω denotes the one-way FR angle in degrees, f_0 is the carrier frequency in Hz, K is a constant of value $2.365 \times 10^4\,[\mathrm{A} \cdot \mathrm{m}^2/\mathrm{kg}]$, B is the magnetic flux density in $\mathrm{Wb/m}^2$, and ψ and θ are the angles the wave-normal makes with the Earth's magnetic field and the downward vertical, respectively. TEC is the total electron content in TEC units (1 TECU = 10^{16} electrons m^{-2}). The "magnetic field factor", $\left[B \cos\psi \cdot \sec\theta\right]_{400}$, is calculated at a height of 400 km.

2.2. System Model

The measured scattering matrix $\mathbf{M}$ in the presence of FR and system errors (channel imbalance, cross-talk and noise) is given by [12],

$$\mathbf{M} = \begin{bmatrix} M_{HH} & M_{VH} \\ M_{HV} & M_{VV} \end{bmatrix} = A\,(r,\theta)\, e^{j\phi} \begin{bmatrix} 1 & \delta_2 \\ \delta_1 & f_1 \end{bmatrix} \cdot \begin{bmatrix} \cos\Omega & \sin\Omega \\ -\sin\Omega & \cos\Omega \end{bmatrix} \cdot \begin{bmatrix} S_{HH} & S_{VH} \\ S_{HV} & S_{VV} \end{bmatrix} \cdot \begin{bmatrix} \cos\Omega & \sin\Omega \\ -\sin\Omega & \cos\Omega \end{bmatrix} \cdot \begin{bmatrix} 1 & \delta_3 \\ \delta_4 & f_2 \end{bmatrix} + \begin{bmatrix} N_1 & N_3 \\ N_2 & N_4 \end{bmatrix} \tag{2}$$

where S_{HH}, S_{HV}, S_{VH} and S_{VV} are the components of the true scattering matrix, f_1 and f_2 denote channel imbalance terms, and δ_i and N_i, $i = 1$–4, are radar cross-talk and additive noise terms, respectively.

Equation (2) can be written in the form

$$\mathbf{M} = A\,(r,\theta)\; e^{j\phi} \cdot \mathbf{GFS} + \mathbf{N} \tag{3}$$

$$\mathbf{G} = \begin{bmatrix} 1 & \delta_4 & \delta_2 & \delta_2\delta_4 \\ \delta_3 & f_2 & \delta_2\delta_3 & f_2\delta_2 \\ \delta_1 & \delta_1\delta_4 & f_1 & f_1\delta_4 \\ \delta_1\delta_3 & f_2\delta_1 & f_1\delta_3 & f_1 f_2 \end{bmatrix} \tag{4}$$

$$\mathbf{F} = \begin{bmatrix} \cos^2\Omega & -\cos\Omega\sin\Omega & \cos\Omega\sin\Omega & -\sin^2\Omega \\ \cos\Omega\sin\Omega & \cos^2\Omega & \sin^2\Omega & \cos\Omega\sin\Omega \\ -\cos\Omega\sin\Omega & \sin^2\Omega & \cos^2\Omega & -\cos\Omega\sin\Omega \\ -\sin^2\Omega & -\cos\Omega\sin\Omega & \cos\Omega\sin\Omega & \cos^2\Omega \end{bmatrix} \quad (5)$$

where $\mathbf{M} = [M_{HH}, M_{HV}, M_{VH}, M_{VV}]^T$ and $\mathbf{S} = [S_{HH}, S_{HV}, S_{VH}, S_{VV}]^T$ denote the measured and true scattering vectors respectively, and $\mathbf{N} = [N_1, N_2, N_3, N_4]^T$ is the additive noise vector.

3. CALIBRATION ALGORITHM

3.1. Signatures of Radar Calibrators

At P-band, passive calibration devices, such as dihedrals and trihedrals, need to be large and become difficult to manufacture and deploy. As a result, ESA is actively investigating the design and analysis of polarimetric active radar calibrators (PARCs) as part of its Phase A studies for BIOMASS. PARCs can be selected to have any polarimetric signature, and in this paper we consider four types, two denoted as PARC_X and PARC_Y [7], that have the signature matrices

$$\mathbf{S}_X = \begin{bmatrix} 0 & 0 \\ 1 & 0 \end{bmatrix} \quad (6)$$

$$\mathbf{S}_Y = \begin{bmatrix} 0 & 1 \\ 0 & 0 \end{bmatrix} \quad (7)$$

together with two others with signature matrices

$$\mathbf{S}_{Gt1} = \begin{bmatrix} 1 & 0 \\ 0 & 0 \end{bmatrix} \quad (8)$$

$$\mathbf{S}_{Gt2} = \begin{bmatrix} 0 & 0 \\ 0 & 1 \end{bmatrix} \quad (9)$$

This notation is chosen because, in principle, the same signatures could be obtained using gridded trihedrals (the classical trihedral with gridded base wires or thin plates; see Fig. 1), which have advantages over the more commonly-used dihedral and trihedral [27]. Such use of a mixture of passive and active radar calibrators for calibrating spaceborne polarimetric SAR systems is discussed in [11, 16, 20, 27, 28].

3.2. Measured Scattering Vectors

Substituting the signature matrices of the passive (9) and active (5) calibrators into the system model (2), and ignoring noise for the moment, gives the following measured scattering vectors for the

different calibrators, where the superscript denotes the type of calibrator:

$$\begin{bmatrix} M_{HH}^{Gt1} \\ M_{HV}^{Gt1} \\ M_{VH}^{Gt1} \\ M_{VV}^{Gt1} \end{bmatrix} = \frac{1}{2}\begin{bmatrix} 1-\delta_2\delta_4+(1+\delta_2\delta_4)\cos 2\Omega+(\delta_4-\delta_2)\sin 2\Omega \\ \delta_3-f_2\delta_2+(\delta_3+f_2\delta_2)\cos 2\Omega+(f_2-\delta_2\delta_3)\sin 2\Omega \\ \delta_1-f_1\delta_4+(\delta_1+f_1\delta_4)\cos 2\Omega+(\delta_1\delta_4-f_1)\sin 2\Omega \\ \delta_1\delta_3-f_1f_2+(f_1f_2+\delta_1\delta_3)\cos 2\Omega+(f_2\delta_1-f_1\delta_3)\sin 2\Omega \end{bmatrix} \quad (10)$$

$$\begin{bmatrix} M_{HH}^{Gt2} \\ M_{HV}^{Gt2} \\ M_{VH}^{Gt2} \\ M_{VV}^{Gt2} \end{bmatrix} = \frac{1}{2}\begin{bmatrix} -(1-\delta_2\delta_4)+(1+\delta_2\delta_4)\cos 2\Omega+(\delta_4-\delta_2)\sin 2\Omega \\ -(\delta_3-f_2\delta_2)+(\delta_3+f_2\delta_2)\cos 2\Omega+(f_2-\delta_2\delta_3)\sin 2\Omega \\ -(\delta_1-f_1\delta_4)+(\delta_1+f_1\delta_4)\cos 2\Omega+(\delta_1\delta_4-f_1)\sin 2\Omega \\ -(\delta_1\delta_3-f_1f_2)+(f_1f_2+\delta_1\delta_3)\cos 2\Omega+(f_2\delta_1-f_1\delta_3)\sin 2\Omega \end{bmatrix} \quad (11)$$

$$\begin{bmatrix} M_{HH}^{X} \\ M_{HV}^{X} \\ M_{VH}^{X} \\ M_{VV}^{X} \end{bmatrix} = \frac{1}{2}\begin{bmatrix} \delta_2+\delta_4+(\delta_2-\delta_4)\cos 2\Omega+(1+\delta_2\delta_4)\sin 2\Omega \\ f_2+\delta_2\delta_3+(\delta_2\delta_3-f_2)\cos 2\Omega+(\delta_3+f_2\delta_2)\sin 2\Omega \\ f_1+\delta_1\delta_4+(f_1-\delta_1\delta_4)\cos 2\Omega+(\delta_1+f_1\delta_4)\sin 2\Omega \\ f_1\delta_3+f_2\delta_1+(f_1\delta_3-f_2\delta_1)\cos 2\Omega+(f_1f_2+\delta_1\delta_3)\sin 2\Omega \end{bmatrix} \quad (12)$$

$$\begin{bmatrix} M_{HH}^{Y} \\ M_{HV}^{Y} \\ M_{VH}^{Y} \\ M_{VV}^{Y} \end{bmatrix} = \frac{1}{2}\begin{bmatrix} \delta_2+\delta_4-(\delta_2-\delta_4)\cos 2\Omega-(1+\delta_2\delta_4)\sin 2\Omega \\ f_2+\delta_2\delta_3-(\delta_2\delta_3-f_2)\cos 2\Omega-(\delta_3+f_2\delta_2)\sin 2\Omega \\ f_1+\delta_1\delta_4-(f_1-\delta_1\delta_4)\cos 2\Omega-(\delta_1+f_1\delta_4)\sin 2\Omega \\ f_1\delta_3+f_2\delta_1-(f_1\delta_3-f_2\delta_1)\cos 2\Omega-(f_1f_2+\delta_1\delta_3)\sin 2\Omega \end{bmatrix} \quad (13)$$

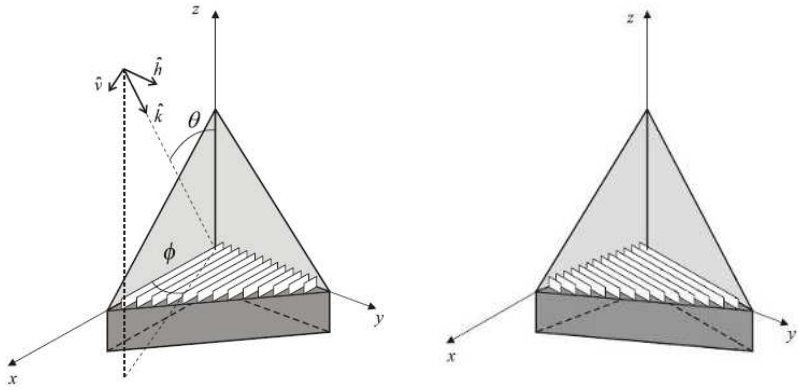

Figure 1. The two forms of gridded trihedral.

3.3. Combination of Calibrators

From (10)–(13), the following relationships between the measurements from different calibrators can be easily derived:

$$\begin{bmatrix} M_{HH}^X + M_{HH}^Y \\ M_{HV}^X + M_{HV}^Y \\ M_{VH}^X + M_{VH}^Y \\ M_{VV}^X + M_{VV}^Y \end{bmatrix} = \begin{bmatrix} \delta_2 + \delta_4 \\ f_2 + \delta_2\delta_3 \\ f_1 + \delta_1\delta_4 \\ f_1\delta_3 + f_2\delta_1 \end{bmatrix} \tag{14}$$

$$\begin{bmatrix} M_{HH}^{Gt1} - M_{HH}^{Gt2} \\ M_{HV}^{Gt1} - M_{HV}^{Gt2} \\ M_{VH}^{Gt1} - M_{VH}^{Gt2} \\ M_{VV}^{Gt1} - M_{VH}^{Gt2} \end{bmatrix} = \begin{bmatrix} 1 - \delta_2\delta_4 \\ \delta_3 - f_2\delta_2 \\ \delta_1 - f_1\delta_4 \\ \delta_1\delta_3 - f_1f_2 \end{bmatrix} \tag{15}$$

$$\begin{bmatrix} M_{HH}^X - M_{HH}^Y \\ M_{HV}^X - M_{HV}^Y \\ M_{VH}^X - M_{VH}^Y \\ M_{VV}^X - M_{VV}^Y \end{bmatrix} = \begin{bmatrix} (\delta_2 - \delta_4)\cos 2\Omega + (1 + \delta_2\delta_4)\sin 2\Omega \\ (\delta_2\delta_3 - f_2)\cos 2\Omega + (\delta_3 + f_2\delta_2)\sin 2\Omega \\ (f_1 - \delta_1\delta_4)\cos 2\Omega + (\delta_1 + f_1\delta_4)\sin 2\Omega \\ (f_1\delta_3 - f_2\delta_1)\cos 2\Omega + (f_1f_2 + \delta_1\delta_3)\sin 2\Omega \end{bmatrix} \tag{16}$$

$$\begin{bmatrix} M_{HH}^{Gt1} + M_{HH}^{Gt2} \\ M_{HV}^{Gt1} + M_{HV}^{Gt2} \\ M_{VH}^{Gt1} + M_{VH}^{Gt2} \\ M_{VV}^{Gt1} + M_{VH}^{Gt2} \end{bmatrix} = \begin{bmatrix} (1 + \delta_2\delta_4)\cos 2\Omega + (\delta_4 - \delta_2)\sin 2\Omega \\ (\delta_3 + f_2\delta_2)\cos 2\Omega + (f_2 - \delta_2\delta_3)\sin 2\Omega \\ (\delta_1 + f_1\delta_4)\cos 2\Omega + (\delta_1\delta_4 - f_1)\sin 2\Omega \\ (f_1f_2 + \delta_1\delta_3)\cos 2\Omega + (f_1\delta_1 - f_1\delta_3)\sin 2\Omega \end{bmatrix} \tag{17}$$

Then (14) and (15) yield the following relationships between the

radar system errors and the measurements:

$$\begin{cases} \delta_1\delta_4 = \left(M_{VH}^X + M_{VH}^Y\right) - f_1 \\ \delta_2\delta_3 = \left(M_{HV}^X + M_{HV}^Y\right) - f_2 \\ \delta_1\delta_3 = f_1 f_2 + \left(M_{VV}^{Gt1} - M_{VV}^{Gt2}\right) \\ \delta_2\delta_4 = 1 - \left(M_{HH}^{Gt1} - M_{HH}^{Gt2}\right) \\ f_1\delta_4 = \delta_1 - \left(M_{VH}^{Gt1} - M_{VH}^{Gt2}\right) \\ f_2\delta_2 = \delta_3 - \left(M_{HV}^{Gt1} - M_{HV}^{Gt2}\right) \end{cases} \tag{18}$$

Using (18), (16) and (17) can be expressed as linear functions of $\sin 2\Omega$ and $\cos 2\Omega$:

$$\begin{cases} a_1 \sin 2\Omega + b_1 \cos 2\Omega = M_{HH}^X - M_{HH}^Y = d_1 \\ a_2 \sin 2\Omega + b_2 \cos 2\Omega = M_{HV}^X - M_{HV}^Y = d_2 \\ a_3 \sin 2\Omega + b_3 \cos 2\Omega = M_{VH}^X - M_{VH}^Y = d_3 \\ a_4 \sin 2\Omega + b_4 \cos 2\Omega = M_{VV}^X - M_{VV}^Y = d_4 \end{cases} \tag{19}$$

$$\begin{cases} a_1 \cos 2\Omega - b_1 \sin 2\Omega = M_{HH}^{Gt1} + M_{HH}^{Gt2} = e_1 \\ a_2 \cos 2\Omega - b_2 \sin 2\Omega = M_{HV}^{Gt1} + M_{HV}^{Gt2} = e_2 \\ a_3 \cos 2\Omega - b_3 \sin 2\Omega = M_{VH}^{Gt1} + M_{VH}^{Gt2} = e_3 \\ a_4 \cos 2\Omega - b_4 \sin 2\Omega = M_{VV}^{Gt1} + M_{VV}^{Gt2} = e_4 \end{cases} \tag{20}$$

and

$$\begin{cases} a_1 = 2 - \left(M_{HH}^{Gt1} - M_{HH}^{Gt2}\right) \\ a_2 = 2\delta_3 - \left(M_{HV}^{Gt1} - M_{HV}^{Gt2}\right) \\ a_3 = 2\delta_1 - \left(M_{VH}^{Gt1} - M_{VH}^{Gt2}\right) \\ a_4 = 2f_1 f_2 + \left(M_{VV}^{Gt1} - M_{VV}^{Gt2}\right) \end{cases} \tag{21}$$

$$\begin{cases} b_1 = \delta_2 - \delta_4 \\ b_2 = \left(M_{HV}^X + M_{HV}^Y\right) - 2f_2 \\ b_3 = 2f_1 - \left(M_{VH}^X + M_{VH}^Y\right) \\ b_4 = f_1\delta_3 - f_2\delta_1 \end{cases} \tag{22}$$

where a_i, $i = 2$–4, and b_i, $i = 1$–4, are unknown coefficients that depend on the radar system errors, while a_1, d_i and e_i, $i = 1$–4, are known coefficients which can be directly derived from the radar calibrator measurements.

3.4. Estimation of FR

It can be deduced from (19) and (20) that

$$\begin{cases} d_1 \sin 2\Omega + e_1 \cos 2\Omega = a_1 \\ d_2 \cos 2\Omega - e_2 \sin 2\Omega = b_2 \\ d_3 \cos 2\Omega - e_3 \sin 2\Omega = b_3 \end{cases} \tag{23}$$

For ideal measurements, this leads to two equivalent solutions for $\cos 2\Omega$ and $\sin 2\Omega$, denoted by the superscript i, $i = 1$–2:

$$\begin{cases} \cos 2\Omega^{(1)} = \frac{a_1 e_2 + b_2 d_1}{d_1 d_2 + e_1 e_2} \\ \sin 2\Omega^{(1)} = \frac{a_1 d_2 - b_2 e_1}{d_1 d_2 + e_1 e_2} \end{cases} \tag{24}$$

$$\begin{cases} \cos 2\Omega^{(2)} = \frac{a_1 e_3 + b_3 d_1}{d_1 d_3 + e_1 e_3} \\ \sin 2\Omega^{(2)} = \frac{a_1 d_3 - b_3 e_1}{d_1 d_3 + e_1 e_3} \end{cases} \tag{25}$$

Since $\cos^2 2\Omega + \sin^2 2\Omega = 1$, the unknown coefficients b_2 and b_3 can be obtained from (24) and (25) as:

$$\begin{cases} b_2 = \frac{-B \pm \sqrt{B^2 - 4AC}}{2A} \\ b_3 = \frac{-B' \pm \sqrt{B'^2 - 4A'C'}}{2A'} \end{cases} \tag{26}$$

where

$$\begin{cases} A = d_1^2 + e_1^2 \\ B = 2a_1 \left(d_1 e_2 - d_2 e_1\right) \\ C = a_1^2 (d_2^2 + e_2^2) - \left(d_1 d_2 + e_1 e_2\right)^2 \end{cases} \tag{27}$$

$$\begin{cases} A' = d_1^2 + e_1^2 \\ B' = 2a_1 \left(d_1 e_3 - d_3 e_1\right) \\ C' = a_1^2 (d_3^2 + e_3^2) - \left(d_1 d_3 + e_1 e_3\right)^2 \end{cases} \tag{28}$$

Hence both b_2 and b_3 have two analytical solutions, but only those resulting in real values of $\cos 2\Omega$ and $\sin 2\Omega$ are acceptable. This condition may not be exactly met in actual measurements because of imperfections in the calibrators, clutter, noise and ambiguities; in this case, the preferred solutions for b_2 and b_3 are those giving imaginary parts of $\cos 2\Omega$ and $\sin 2\Omega$ that are close to zero.

Consequently, we can construct the complex variables Z_i, $i = 1$–2, given by

$$Z_i = \cos 2\Omega^{(i)} + j \sin 2\Omega^{(i)}, \quad i = 1{-}2 \tag{29}$$

which yield two alternative FR estimates:

$$\hat{\Omega}^{(i)} = \frac{1}{2} \arg\{\mathrm{Z}_i\}, \quad i = 1{-}2 \tag{30}$$

Both $\hat{\Omega}^{(1)}$ and $\hat{\Omega}^{(2)}$ take values from $-\pi/2$ to $\pi/2$ (so have an ambiguity of π), and have equivalent accuracy. Hence we can half the error variance by estimating FR as

$$\hat{\Omega} = \frac{1}{2} \left(\hat{\Omega}^{(1)} + \hat{\Omega}^{(2)} \right). \tag{31}$$

3.5. Correcting FR Estimation Ambiguity Using TEC Data

The FR estimates in (30) and (31) lie between $\pm\pi/2$, leading to an ambiguity of $\pm k\pi$. However, this can be removed by using (1) to provide an independent estimate of FR, where TEC is given by the global ionospheric TEC maps estimated by the Global Navigation Satellite System (GNSS) and use is made of the IGRF10 model for the Earth's magnetic field [12]. The International GNSS Service provides bi-hourly global TEC maps with grid-points spaced 5° in longitude and 2.5° in latitude [12, 29], with an overall root mean square (RMS) errors of 3–5 TECU [29, 30].

Hence, an unambiguous FR estimator is given by [25]:

$$\hat{\Omega}^F = \hat{\Omega} + \text{round}\left(\frac{\hat{\Omega}_{GNSS} - \hat{\Omega}}{\pi/2}\right) \cdot \frac{\pi}{2} \tag{32}$$

where round$(\cdot)$ denotes rounding to the nearest integer, $\hat{\Omega}_{GNSS}$ is the FR predicted from GNSS TEC data and $\hat{\Omega}$ is taken from (31). However, for reasons discussed in Section 5, the use of GNSS data may not be necessary, since achieving sufficient accuracy in the system error estimates appears to require calibration sites deployed at the magnetic equator, where FR is nearly zero, or an independent measurement of TEC using a two-frequency transmitter on the satellite with a receiver at the calibration sites.

3.6. Estimation of Radar System Errors

The estimates of the radar system errors can be calculated in terms of the FR estimate $\hat{\Omega}^F$. According to (22) and (26), the channel imbalance estimates can be written as

$$\begin{cases} \hat{f}_1 = \frac{1}{2}\Big[\big(M_{VH}^X - M_{VH}^Y\big)\cos 2\hat{\Omega}^F - \big(M_{VH}^{Gt1} + M_{VH}^{Gt2}\big)\sin 2\hat{\Omega}^F + \big(M_{VH}^X + M_{VH}^Y\big)\Big] \\ \hat{f}_2 = \frac{1}{2}\Big[\big(M_{HV}^{Gt1} + M_{HV}^{Gt2}\big)\sin 2\hat{\Omega}^F - \big(M_{HV}^X - M_{HV}^Y\big)\cos 2\hat{\Omega}^F + \big(M_{HV}^X + M_{HV}^Y\big)\Big] \end{cases} \tag{33}$$

Similarly, the cross-talk estimates can be derived on the basis of (19)–(22), and are given by

$$\begin{cases} \hat{\delta}_1 = \frac{1}{2}\Big[\big(M_{VH}^X - M_{VH}^Y\big)\sin 2\hat{\Omega}^F + \big(M_{VH}^{Gt1} + M_{VH}^{Gt2}\big)\cos 2\hat{\Omega}^F \\ \qquad + \big(M_{VH}^{Gt1} - M_{VH}^{Gt2}\big)\Big] \\ \hat{\delta}_3 = \frac{1}{2}\Big[\big(M_{HV}^X - M_{HV}^Y\big)\sin 2\hat{\Omega}^F + \big(M_{HV}^{Gt1} + M_{HV}^{Gt2}\big)\cos 2\hat{\Omega}^F \\ \qquad + \big(M_{HV}^{Gt1} - M_{HV}^{Gt2}\big)\Big] \end{cases} \tag{34a}$$

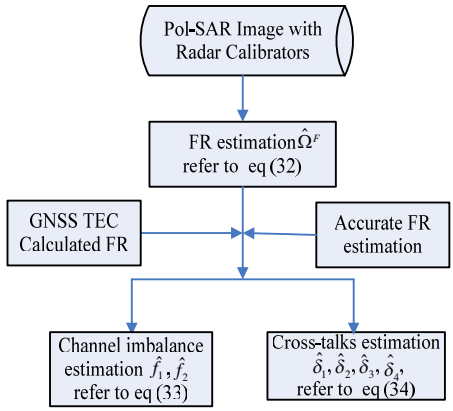

Figure 2. Flowchart of the calibration scheme.

$$\begin{cases} \hat{\delta}_2 = \frac{1}{2}\left[\left(M_{HH}^X - M_{HH}^Y\right)\cos 2\hat{\Omega}^F - \left(M_{HH}^{Gt1} + M_{HH}^{Gt2}\right)\sin 2\hat{\Omega}^F \right. \\ \qquad \left. + \left(M_{HH}^X + M_{HH}^Y\right)\right] \\ \hat{\delta}_4 = \frac{1}{2}\left[\left(M_{HH}^{Gt1} + M_{HH}^{Gt2}\right)\sin 2\hat{\Omega}^F - \left(M_{HH}^X - M_{HH}^Y\right)\cos 2\hat{\Omega}^F \right. \\ \qquad \left. + \left(M_{HH}^X + M_{HH}^Y\right)\right] \end{cases} \tag{34b}$$

The full calibration scheme is summarized in Fig. 2. It is clear that accurate estimation of FR is of paramount importance if accurate estimates of both channel imbalance and cross-talk are to be obtained.

3.7. Accuracy Analysis of Radar System Error Estimation

The FR estimation error $\Delta\Omega^F = \hat{\Omega}^F - \Omega^F$, where Ω^F denotes the true FR value, will lead to estimation errors for the radar system errors given by

$$\begin{cases} \Delta f_1 = -\sin\Delta\Omega^F\left[\left(M_{VH}^X - M_{VH}^Y\right)\sin\left(2\Omega^F + \Delta\Omega^F\right) \right. \\ \qquad \left. + \left(M_{VH}^{Gt1} + M_{VH}^{Gt2}\right)\cos\left(2\Omega^F + \Delta\Omega^F\right)\right] \\ \Delta f_2 = \sin\Delta\Omega^F\left[\left(M_{HV}^X - M_{HV}^Y\right)\sin\left(2\Omega^F + \Delta\Omega^F\right) \right. \\ \qquad \left. + \left(M_{HV}^{Gt1} + M_{HV}^{Gt2}\right)\cos\left(2\Omega^F + \Delta\Omega^F\right)\right] \end{cases} \tag{35a}$$

$$\begin{cases} \Delta\delta_1 = \sin\Delta\Omega^F\left[\left(M_{VH}^X - M_{VH}^Y\right)\cos\left(2\Omega^F + \Delta\Omega^F\right) \right. \\ \qquad \left. - \left(M_{VH}^{Gt1} + M_{VH}^{Gt2}\right)\sin\left(2\Omega^F + \Delta\Omega^F\right)\right] \\ \Delta\delta_3 = \sin\Delta\Omega^F\left[\left(M_{HV}^X - M_{HV}^Y\right)\cos\left(2\Omega^F + \Delta\Omega^F\right) \right. \\ \qquad \left. - \left(M_{HV}^{Gt1} + M_{HV}^{Gt2}\right)\sin\left(2\Omega^F + \Delta\Omega^F\right)\right] \end{cases} \tag{35b}$$

$$\begin{cases} \Delta\delta_2 = -\sin\Delta\Omega^F \left[\left(M_{HH}^X - M_{HH}^Y \right) \sin(2\Omega^F + \Delta\Omega^F) \right. \\ \qquad \left. + \left(M_{HH}^{Gt1} + M_{HH}^{Gt2} \right) \cos(2\Omega^F + \Delta\Omega^F) \right] \\ \Delta\delta_4 = \sin\Delta\Omega^F \left[\left(M_{HH}^X - M_{HH}^Y \right) \sin\left(2\Omega^F + \Delta\Omega^F \right) \right. \\ \qquad \left. + \left(M_{HH}^{Gt1} + M_{HH}^{Gt2} \right) \cos\left(2\Omega^F + \Delta\Omega^F \right) \right] \end{cases} \tag{35c}$$

where Δf_1 and Δf_2 denote channel imbalance estimation errors and $\Delta\delta_1$, $\Delta\delta_2$, $\Delta\delta_3$ and $\Delta\delta_4$ stand for cross-talk estimation errors.

From (14)–(17), Δf_1 and Δf_2 would be expected to have similar statistics, as would the cross-talk pairs $\Delta\delta_1$, $\Delta\delta_3$ and $\Delta\delta_2$, $\Delta\delta_4$. This is confirmed by the simulations shown in Section 4.1 (e.g., see Figs. 5 & 6).

4. SIMULATIONS AND DISCUSSION

In this section, we assess the performance of the calibration scheme using Monte Carlo simulation. In Section 4.1, the calibrators are treated as perfect, but we permit errors in the estimate of FR. However, calibrator characteristics may deviate from the ideal because of imperfect construction, inaccurate alignment relative to the satellite track, etc. The ensuing errors are referred to as average polarimetric noise (APN), and their effects on calibration accuracy are quantified in Section 4.2. All estimates in Sections 4.1 and 4.2 assume that system noise, in which we include clutter and ambiguities, is negligible, but this depends on the construction of the calibrators and how they are deployed. Hence, in Section 4.3, we assess the performance of the calibration scheme as a function of the signal-to-noise ratio (SNR), both with and without APN.

4.1. System Error Analysis without Calibrator Error

The estimate of FR is given by (32). Without calibrator error, this is nominally exact, but it is helpful for later analysis to first derive the effects of error in the FR value on the statistical properties of the system error estimates. In the simulations, we allow the channel imbalance amplitudes to range from -3 dB to 3 dB, the cross-talk amplitudes to range from -40 dB to -10 dB, and the phase errors in both channel imbalances and cross-talks to range over $\pm\pi$. We also carried out simulations where the cross-talk amplitudes were restricted to the more realistic range -40 dB to -25 dB. These are discussed in the text, but all figures are derived using the -40 dB to -10 dB range.

Figures 3–6 show the mean and standard deviation (SD) of the errors in the estimates of the radar system terms as functions of the FR estimation error (varying within $\pm 1^\circ$). The FR error is seen to

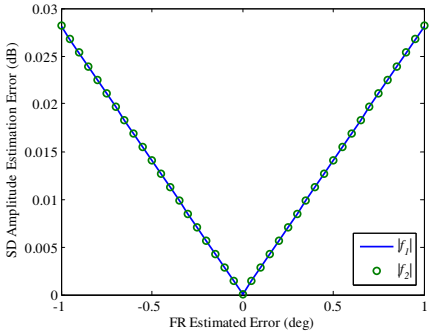

Figure 3. SD of the amplitude error of the channel imbalance terms as a function of FR estimation error.

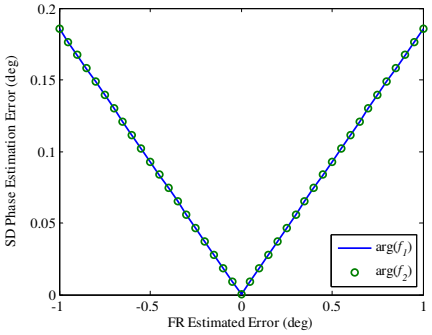

Figure 4. SD of the phase error of the channel imbalance terms as a function of FR estimation error.

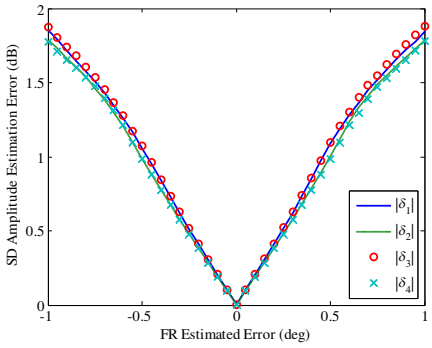

Figure 5. SD of the amplitude error of the cross-talk terms as a function of FR estimation error.

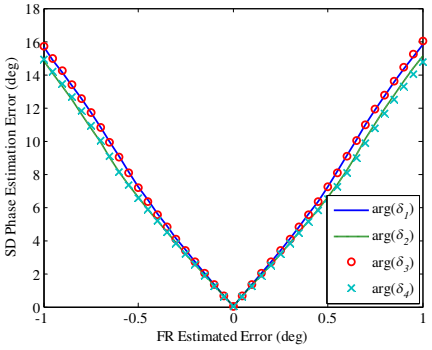

Figure 6. SD of the phase error of the cross-talk terms as a function of FR estimation error.

have little effect on the channel imbalance estimates (see Figs. 3 & 4), but the cross-talk estimates degrade severely as the error increases. For larger FR errors, the estimates of the cross-talk amplitudes become significantly biased and have a large SD (Fig. 5). The cross-talk phase error estimates are nearly unbiased, but their SD grows very rapidly as the FR error increases (Fig. 6). For the SD of the error in the cross-talk phases to be less than 5°, the FR error must not exceed 0.36°, and to keep it below 1° requires the FR error to be less than 0.07° (Fig. 6); these are strong constraints on the FR estimator.

4.2. System Error Analysis with Calibrator Noise

The error models for the calibration targets are given by [15]

$$\mathbf{S}'_{Gt1} = \begin{bmatrix} 1 & \delta_{Gt1} \\ \delta_{Gt1} & \delta_{Gt1}^2 \end{bmatrix} \tag{36a}$$

$$\mathbf{S}'_{Gt2} = \begin{bmatrix} \delta_{Gt2}^2 & \delta_{Gt2} \\ \delta_{Gt2} & 1 \end{bmatrix} \tag{36b}$$

$$\mathbf{S}'_{X} = \begin{bmatrix} \delta_X & \delta_X^2 \\ 1 & \delta_X \end{bmatrix} \tag{36c}$$

$$\mathbf{S}'_{Y} = \begin{bmatrix} \delta_Y & 1 \\ \delta_Y^2 & \delta_Y \end{bmatrix} \tag{36d}$$

where δ_{Gt1}, δ_{Gt2}, δ_X and δ_Y are complex numbers representing the APN of the calibrators. The form of these error matrices would be unchanged if the PARCs were replaced by gridded trihedrals.

To evaluate the impact of APN on the calibration scheme, we assume for simplicity that $|\delta_{Gt1}| = |\delta_{Gt2}| = |\delta_X| = |\delta_Y|$, and allow these values to range from -60 to -20 dB; $\arg(\delta_{Gt1})$, $\arg(\delta_{Gt2})$, $\arg(\delta_X)$ and $\arg(\delta_Y)$ are taken to be uniformly distributed over $\pm\pi$.

The FR estimated from the calibration scheme is nearly unbiased for all values of APN, but Fig. 7 illustrates that its SD, σ_{FR}, increases rapidly with APN; an APN error of -40 dB will yield a σ_{FR} of 1°. Figs. 5 and 6 indicate that this will lead to cross-talks with amplitude errors whose SD is 1.8 dB, and phase errors whose SD is 16°. Even if APN is as low as -60 dB, σ_{FR} is 0.28°, corresponding to a cross-talk phase estimation error with SD 4°. Hence a method that estimates FR from the calibrator responses will not yield sufficient accuracy to

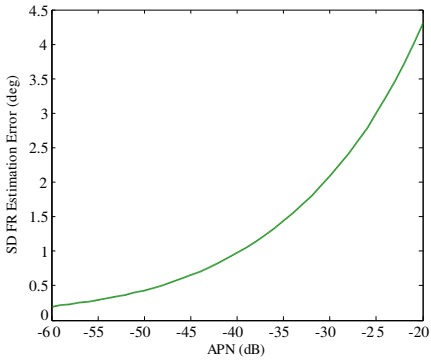

Figure 7. SD of the FR estimation error as a function of APN.

calibrate the system, and independent methods to estimate FR are needed; these are discussed in Section 5, and for the remainder of the paper we assume that such methods are available.

The estimation errors in channel imbalance and cross-talk will depend on both the accuracy of FR estimate and on APN. Simulations were performed to assess this, with σ_{FR} fixed at 0°, 0.1° and 0.3°. The effect on the estimate of the channel imbalance is small under all conditions, and only for APN as large as −25 dB did the SD of its estimated phase error become as large as 1°. In contrast, the amplitude and phase estimates of the cross-talks, despite being nearly unbiased for APN less than −25 dB, have SDs that depend strongly on σ_{FR} (see Figs. 8 and 9, which show these SDs when σ_{FR} is 0.1° and 0.3°). Even for APN as small as −60 dB, σ_{FR} has to be less than 0.3° to keep the SD of all the cross-talk amplitude errors below 1 dB (Fig. 8). Even more stringently, σ_{FR} has to be reduced to 0.1° to keep the cross-talk phase SD within acceptable bounds (Fig. 9). In this case, for an APN of −60 dB, the cross-talk phase SD is around 2.72° when the cross-talk amplitude is kept below −25 dB, and 1.53° when it is kept below −10 dB, reflecting the fact that cross-talk can be measured more accurately when it is larger.

4.3. The Effects of Clutter and Noise on Calibration Accuracy

The analysis in previous sections has assumed that the calibrators can be constructed and located in such a way that noise and clutter

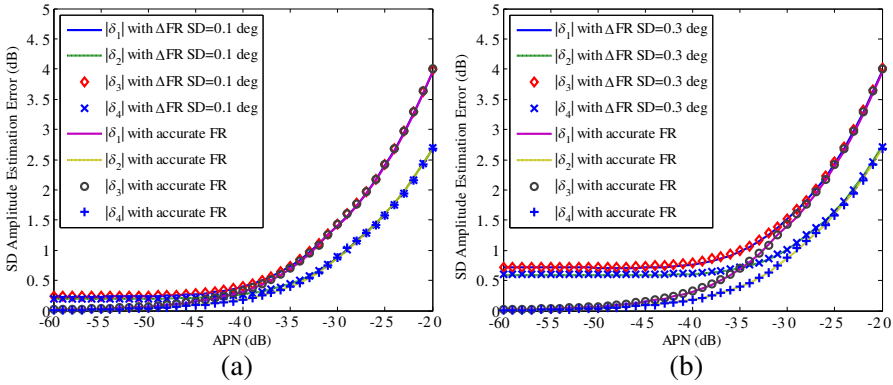

Figure 8. (a) SD of the amplitude error of the cross-talk terms as a function of APN. (b) SD of the amplitude error of the cross-talk terms as a function of APN.

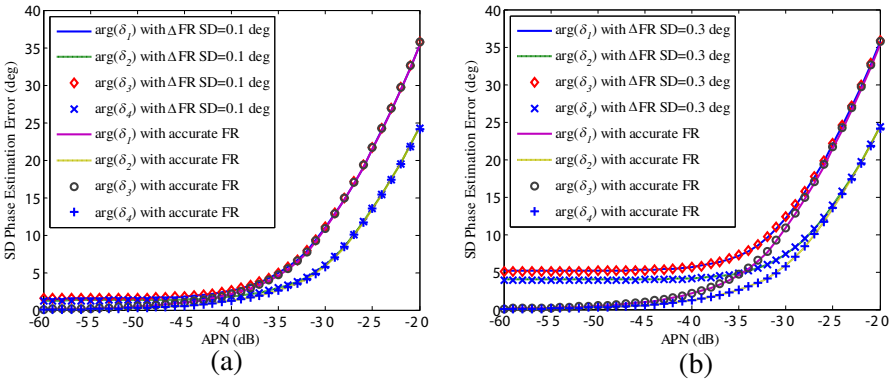

Figure 9. (a) SD of the phase error of the cross-talk terms as a function of APN. (b) SD of the phase error of the cross-talk terms as a function of APN.

can be neglected. However, the 6 MHz bandwidth allowable under ITU regulations for a spaceborne P-Band SAR corresponds to a slant range spatial resolution of 25 m, or 50 m ground range resolution at an incidence angle of 30°. Hence, to keep the clutter and ambiguities to an acceptable level, the areas of low backscatter surrounding the calibrators need be quite large and carefully chosen. To assess how critical this requirement is, or equivalently how large the SNR needs to be, the performance of the calibration was first evaluated for different levels of SNR, under the assumption of no APN error. This assessment was based on 100,000 Monte Carlo simulations for each value of SNR ranging from 20 dB to 60 dB in steps of 1 dB, and assumed the clutter and noise to be white Gaussian.

Under the conditions of the simulation, values of FR estimated from the calibrator measurements were insufficiently accurate; even for an SNR of 60 dB, σ_{FR} was approximately 1°, which leads to unacceptably large cross-talk errors (see Figs. 5 and 6). Hence, as in the APN analysis, we assume that the estimate of FR is derived independently, and the simulations used σ_{FR} values fixed at 0°, 0.1° and 0.3°. The SNR has negligible effect on the amplitude of the channel imbalance, but needs to exceed 33 dB to keep the phase of the channel imbalance error below 0.5° when the cross-talk amplitudes are constrained to be less than −25 dB (or 20 dB for cross-talk amplitudes less than −10 dB). The effects on the cross-talk are more serious, as shown in Fig. 10 for the amplitude errors and Fig. 11 for the phase errors. Fig. 10(b) indicates that σ_{FR} has to be less than 0.3° to keep the SD of the cross-talk amplitudes below 1 dB. When $\sigma_{FR} = 0.1°$,

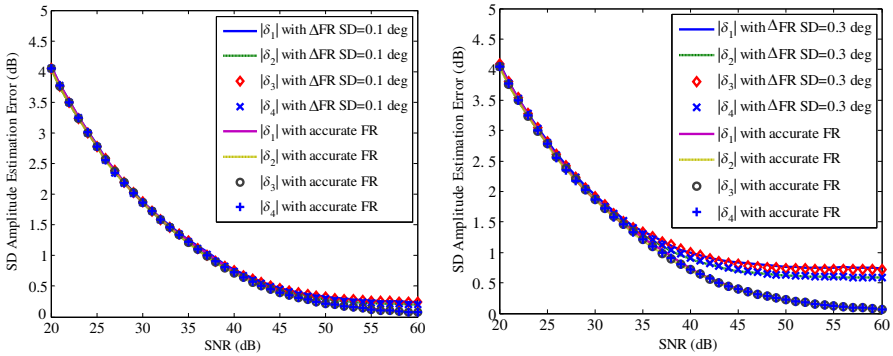

Figure 10. (a) SD of the amplitude error of the cross-talk terms as a function of SNR. (b) SD of the amplitude error of the cross-talk terms as a function of SNR.

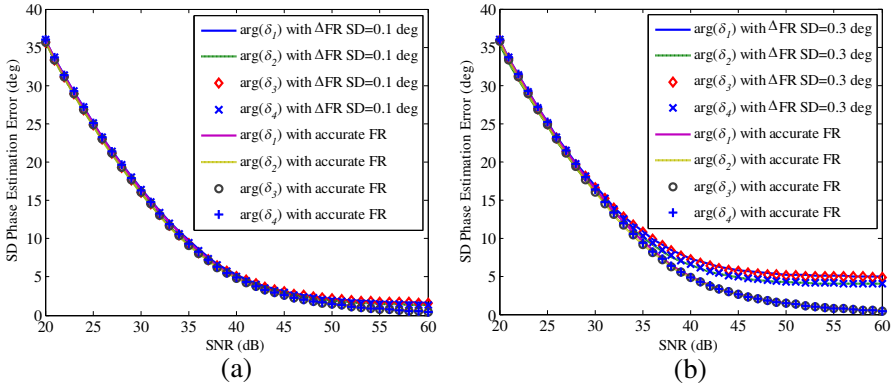

Figure 11. (a) SD of the phase error of the cross-talk terms as a function of SNR. (b) SD of the phase error of the cross-talk terms as a function of SNR.

meeting this condition requires SNR to exceed 43 dB when the cross-talk amplitudes are less than −25 dB (or 37 dB when the cross-talk amplitudes are less than −10 dB). Fig. 12 reinforces the need for σ_{FR} to be 0.1° or less, since only then can the SDs of the cross-talk phase errors be held to acceptable values. When the SNR is 60 dB, Fig. 11(a) shows that the phase error SD is 2.84° when the cross-talk amplitudes are constrained to be less than −25 dB (or 1.6° for less than −10 dB).

In practice, system errors have to be estimated in the simultaneous presence of APN and system noise. Figs. 12–13 illustrate results from

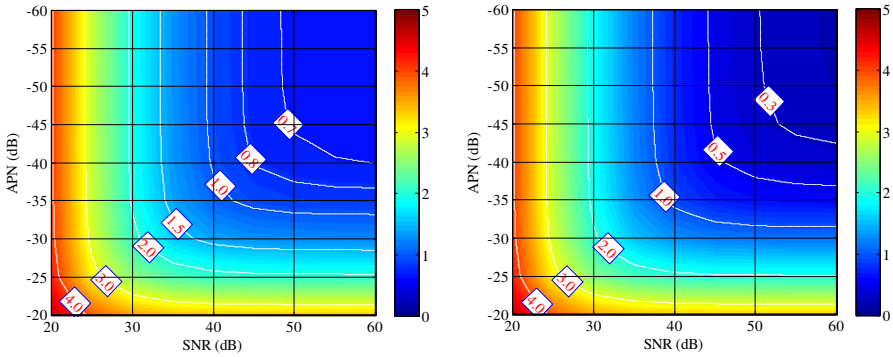

Figure 12. (a) SD of the amplitude error of cross-talk terms as a function of APN and SNR for $\sigma_{FR} = 0.3°$. The color bar is given in dB. (b) SD of the amplitude error of the cross-talk terms as a function of APN and SNR for $\sigma_{FR} = 0.1°$. The color bar is given in dB.

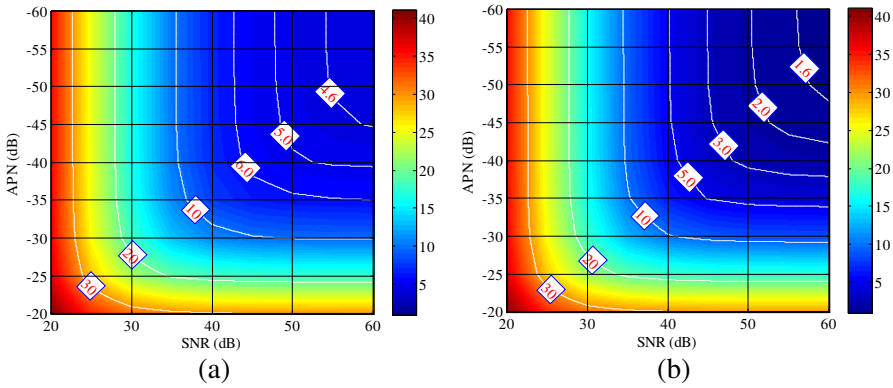

Figure 13. (a) SD of the phase error of cross-talk terms as a function of APN and SNR for $\sigma_{FR} = 0.3°$. The color bar is given in degrees. (b) SD of the phase error of cross-talk terms as a function of APN and SNR for $\sigma_{FR} = 0.1°$. The color bar is given in degrees.

Monte Carlo simulations under these conditions, with the channel imbalance amplitudes ranging from -3 dB to 3 dB, the cross-talk amplitudes ranging from -40 dB to -10 dB, and the phase errors in both channel imbalances and cross-talks ranging over $\pm\pi$. Each figure shows isoclines for cross-talk error statistics as SNR ranges from 20 to 60 dB and APN ranges from -20 to -60 dB. Results for $\sigma_{FR} = 0.3°$ and $0.1°$ are shown. Essentially, each isocline consists of a vertical part (i.e.,

independent of SNR) and horizontal part (i.e., independent of APN). Hence improving the estimates cannot be achieved by just reducing APN or increasing SNR separately. APN and SNR are optimally matched at the roll-off between the vertical and the horizontal parts, and the values quoted below are based on this.

The errors in the amplitude and phase of the channel imbalance (not shown) are negligible as long as APN < -35 dB and SNR > 35 dB. However, Fig. 12(a) shows that keeping the SD of cross-talk amplitude errors below 1 dB requires APN < -37 dB and SNR > 42 dB when $\sigma_{FR} = 0.3°$; the SD is reduced to about 0.8 dB for the same values of APN and SNR when $\sigma_{FR} = 0.1°$ (Fig. 12(b)). The constraints are more severe for the estimate of the cross-talk phase; Fig. 13 shows that σ_{FR} has to be reduced to 0.1° to keep its SD within acceptable bounds. The values of APN and SNR needed to keep the phase SD below a range of values is given in Table 1.

Table 1. Values of APN and SNR needed to keep the SD of the cross-talk phase error below a range of values.

SD of cross-talk phase error (degrees)	APN (dB)	SNR(dB)
10.0	−28	34
4.0	−38	45
3.0	−40	48
2.0	−45	53
1.5	−60	60

Table 2. The corresponding accuracy in the channel imbalance and cross-talk terms for FR accuracies of 0.1° and 0.3°, under the needed SNR and APN to measure cross-talk phase accuracy of 10° (namely, SNR = 34 dB and APN = −28 dB @$\sigma_{FR} = 0.1°$, see Table 1).

	$\sigma_{FR} = 0.1°$	$\sigma_{FR} = 0.3°$
SD of channel imbalance amplitude (dB)	0.06	0.07
SD of channel imbalance phase (deg)	0.44	0.48
SD of cross-talk amplitude (dB)	1.38	1.45
SD of cross-talk phase (deg)	10°	11°

5. DISCUSSION AND CONCLUSIONS

Spaceborne SAR systems are much more stable in time and space than airborne systems, and should need less frequent estimates of calibration errors. Hence accurate repeated measurements of radar system errors at a small number of dedicated calibration sites are likely to be sufficient to give acceptable calibration of the whole dataset.

Taking this as a premise, this paper proposes a calibration scheme to measure the system errors in the presence of Faraday rotation. This involves four PARCs selecting for the HH, VV, HV and VH channels (the PARCs selecting for the HH and VV channels could in principle be replaced by equivalent gridded trihedrals), supplemented by independent estimates of TEC from the GNSS. Several calibrator sites would need to be positioned across the swath to account for possible variation in system errors with look angle, though calibration sites at different ranges would not need to be contained in the same image. Also, if multiple calibration sites were distributed along the satellite track at similar locations in the swath, and the system errors are independent of latitude, then averaging of estimates will reduce their variance.

Theoretical analysis and simulation demonstrate that a critical issue is the estimate of FR. In the absence of calibrator error, FR can be very accurately estimated using the measurements from the calibration devices, leading to nearly perfect estimates of the system errors. However, calibrator errors, system noise and ambiguities can significantly degrade FR estimation accuracy, leading to large relative amplitude and phase errors in the estimated cross-talks. The simulations indicate that the APN error must be less than -60 dB to give accurate simultaneous estimates of FR and cross-talk, and even an SNR as large as 60 dB leads to errors in the cross-talk phase of several degrees.

Two possibilities seem available to avoid this impasse. The first is to deploy calibration sites at the magnetic equator, where the Faraday rotation is zero. This will be effective if the orbital and magnetic field geometry is known precisely enough to ensure that Faraday rotation is negligible. However, if there is a risk that the system errors have a dependence on latitude (perhaps due to changes in solar illumination conditions), this will not be sufficient. A second approach is to make an independent measurement of TEC using a two-frequency transmitter on the satellite with a receiver at the calibration sites. The accuracy of the TEC estimate derived from this approach can be as high as 0.1 TECU [31].

The associated accuracy of the FR estimate can be approximated

using the expression for Faraday rotation given in [21]:

$$\Omega \approx 3.583 \times (\sin \Lambda + 0.037) \times \mathrm{TEC} \tag{37}$$

where Λ is latitude and TEC is measured in TEC units (TECU). This is derived under the simplifying assumption of a dipolar magnetic field and coincident magnetic and geographic axes, and for a radar operating at 435 MHz with look angle 28° and an orbital inclination of 98°. Hence the SD of the FR estimate increases with latitude; for a TEC accuracy of 0.1 TECU it reaches 0.1° at latitude of 15°, growing to approximately 0.36° at 75°N. Hence, even with an independent line-of-sight measurement of TEC, the calibration sites still need to be located at low latitudes to give accurate estimates of the cross-talk phase, unless more accurate ways to provide independent estimates of TEC can be formulated.

Given such ancillary knowledge of FR, adequate estimates of cross-talk phase (the most sensitive variable) can be derived. In particular, Table 2 indicates the levels of SNR and APN needed to measure the cross-talk phase to an accuracy of 10°, and the corresponding accuracy in the cross-talk amplitude and channel imbalance terms, for FR accuracies of 0.1° and 0.3°. Note that, since cross-talk is taken to be small, these accuracies are likely to be adequate as regards their impact on the polarimetric variables. Such requirements on SNR and APN are likely to be achievable.

One important caveat is needed with regards to the conclusions above. In this paper, we have been exclusively concerned with establishing the limits on our capability to measure system errors using calibration devices. The stringent demands on the FR estimates arise largely because the system errors are likely to be very small, hence the perturbation of the measurements caused by FR lead to large relative errors in the estimates. However, if the system errors are small, such errors may have little impact on the accuracy of the primary measurements by the BIOMASS system, which include the scattering matrix and polarimetric interferometric variables. Hence establishing the true demands on calibration accuracy requires the analysis in this paper to be embedded in a full analysis of the performance of the BIOMASS system. An opportunity to do so is likely to arise from the end-to-end BIOMASS simulator currently under development for ESA.

ACKNOWLEDGMENT

The authors would like to thank the reviewers for their comments and suggestions, which helped us to improve the paper. This work described in the paper was supported by the National Science Foundation of China (NSFC) under Grant 60602045.

REFERENCES

1. Balzter, H., M. Davidson, T. Le Toan, P. Paillou, K. Papathanassiou, S. Plummer, S. Quegan, F. Rocca, S. S. Saatchi, H. Shugart, and L. Ulander, "BIOMASS report for assessment," ESA SP 1313/2, European Space Agency, 2008.
2. Hasar, U. C. and O. Simsek, "A simple approach for evaluating the reciprocity of materials without using any calibration standard," *Progress In Electromagnetics Research*, Vol. 91, 139–152, 2009.
3. Dlugosz, T. and H. Trzaska, "A new calibration method for non-stationary electromagnetic fields measurements," *Journal of Electromagnetic Waves and Applications*, Vol. 23, No. 17–18, 2471–2480, 2009.
4. Litman, A., J.-M. Geffrin, and H. Tortel, "On the calibration of a multistatic scattering matrix measured by a fixed circular array of antennas," *Progress In Electromagnetics Research*, Vol. 110, 1–21, 2010.
5. García-Tuñón, I., J. L. Rodríguez, F. Obelleiro, and M. G. Araújo, and J. M. Taboada, "Insensitive environment calibration procedure for an instrumental radar," *Journal of Electromagnetic Waves and Applications*, Vol. 24, No. 16, 2165–2177, 2010.
6. Ma, L., Z.-F. Li, and G. S. Liao, "System error analysis and calibration methods for multi-channel SAR," *Progress In Electromagnetics Research*, Vol. 112, 309–327, 2011.
7. Freeman, A., Y. Shen, and C. L. Werner, "Polarimetric SAR calibration experiment using active radar calibrators," *IEEE Trans. Geosci. Remote Sens.*, Vol. 28, No. 7, 224–240, Mar. 1990.
8. Freeman, A., "SAR calibration: An overview," *IEEE Trans. Geosci. Remote Sens.*, Vol. 30, No. 11, 1107–1121, 1992.
9. Quegan, S., "A unified algorithm for phase and cross-talk calibration of polarimetric data — Theory and observations," *IEEE Trans. Geosci. Remote Sens.*, Vol. 32, No. 1, 89–99, 1994.
10. Fujita, M., T. Masuda, Y. Fujino, and M. Satake, "Polarimetric calibration of the SIR-C C-band channel using active radar calibrators and polarization selective dihedrals," *IEEE Trans. Geosci. Remote Sens.*, Vol. 36, 1872–1878, Nov. 1998.
11. Yueh, S. H., J. A. Kong, and R. T. Shin, "Calibration of polarimetric radars using in-scene reflectors," *Progress In Electromagnetics Research,* Vol. 03, 451–510, 1990.
12. Meyer, F. J. and J. B. Nicoll, "Prediction, detection, and correction of Faraday rotation in full-polarimetric L-band SAR data," *IEEE Trans. Geosci. Remote Sens.*, Vol. 46, No. 10, 3076–

3086, Oct. 2008.

13. Sandberg, G., L. Eriksson, and L. Ulander, "Measurements of Faraday rotation using polarimetric PALSAR images," *IEEE Geosci. Remote Sens. Lett.*, Vol. 6, No. 1, 142–146, Dec. 2009.
14. Freeman, A., X.-Q. Pi, and B. Chapman, "Calibration of PalSAR polarimetric data," *Proc. POLinSAR 2009*, Frascati, Italy, Jan. 2009.
15. Fujita, M., "Development of a retrodirective PARC for ALOS/PALSAR calibration," *IEEE Trans. Geosci. Remote Sens.*, Vol. 41, No. 10, 2177–2186, Oct. 2003.
16. Fujita, M., "Polarimetric calibration of space SAR data subject to Faraday rotation — A three target approach," *Proc. IEEE IGARSS2005*, Vol. 8, 5497–5500, Jul. 25–29, 2005.
17. Takeshiro, A., T. Furuya, and H. Fukuchi, "Verification of polarimetric calibration method including Faraday rotation compensation using PALSAR data," *IEEE Trans. Geosci. Remote Sens.*, Vol. 47, No. 12, 3960–3968, Dec. 2009.
18. Kimura, H., "Calibration of polarimetric PALSAR imagery affected by Faraday rotation using polarization orientation," *IEEE Trans. Geosci. Remote Sens.*, Vol. 47, No. 12, 3943–3950, Dec. 2009.
19. Shimada, M., O. Isoguchi, T. Tadono, and K. Isono, "PALSAR radiometric and geometric calibration," *IEEE Trans. Geosci. Remote Sens.*, Vol. 47, No. 12, 3915–3932, Dec. 2009.
20. Touzi, R. and M. Shimada, "Polarimetric PALSAR calibration," *IEEE Trans. Geosci. Remote Sens.*, Vol. 47, No. 12, 3951–3959, Dec. 2009.
21. Wright, P. A., S. Quegan, N. S. Wheadon, and C. D. Hall, "Faraday rotation effects on L-band spaceborne data," *IEEE Trans. Geosci. Remote Sens.*, Vol. 41, No. 12, 2735–2744, Dec. 2003.
22. Jin, Y.-Q., "Polarimetric scattering modeling and information retrieval of SAR remote sensing — A review of FDU work," *Progress In Electromagnetics Research*, Vol. 104, 333–384, 2010.
23. Xu, Z.-W., J. Wu, and Z.-S. Wu, "A survey of ionospheric effects on space-based radar," *Waves in Random Media*, Vol. 14, No. 12, 189–272, Apr. 2004.
24. Qi, R.-Y. and Y.-Q. Jin, "Analysis of the effects of Faraday rotation on spaceborne polarimetric SAR observations at P-band," *IEEE Trans. Geosci. Remote Sens.*, Vol. 45, No. 5, 1115–1122, May 2007.

25. Chen, J. and S. Quegan, "Improved estimators of Faraday rotation in spaceborne polarimetric SAR data," *IEEE Geosci. Remote Sens. Lett.*, Vol. 7, No. 4, Oct. 2010.
26. Freeman, A., "Calibration of linearly polarized polarimetric SAR data subject to Faraday rotation," *IEEE Trans. Geosci. Remote Sens.*, Vol. 42, No. 8, 1617–1624, Aug. 2004.
27. Sheen, D. R., E. L. Johansen, L. P. Elenbogen, and E. S. Kasischke, "The gridded trihedral: A new polarimetric SAR calibration reflector," *IEEE Trans. Geosci. Remote Sens.*, Vol. 30, No. 6, 1149–1153, Nov. 1992.
28. Lavalle, M., B. Rosich, T. Ainsworth, E. Pottier, and D. Solimini, "Calibration of dual-pol SAR data: A possible approach for Sentinel-1," *Proc. POLinSAR 2009*, Frascati, Italy, Jan. 2009.
29. Sekido, M., T. Kondo, E. Kawai, and M. Imae, "Evaluation of GPS-based ionospheric TEC map by comparing with VLBI data," *Radio Sci.*, Vol. 38, No. 4, 8-1–8-22, Jul. 2003.
30. Mandrake, L., B. Wilson, C. Wang, G. Hajj, A. Mannucci, and X. Pi, "A performance evaluation of the operational Jet Propulsion Laboratory/University of Southern California global assimilation ionospheric model (JPL/USC GAIM)," *J. Geophys. Res.*, 110, A12306, Dec. 2005.
31. Salós, D., C. Macabiau, A. Martineau, B. Bonhoure, and D. Kubrak, "Nominal GNSS pseudorange measurement model for vehicular urban applications," *Position Location and Navigation Symposium (PLANS), 2010 IEEE/ION*, 806–815, 2010.